Journal of Analytical and Applied Pyrolysis 193 (2026) 107473

Contents lists available at ScienceDirect

Journal of Analytical and Applied Pyrolysis

journal homepage: www.elsevier.com/locate/jaap

Plasma-chemical mechanism and multi-objective optimization of microwave discharge plasma-driven methane pyrolysis enabling scalable carbon-negative hydrogen and high-quality graphene co-production

Wenshuo Wang [a], Zhoulin Liu [a,b], Baoxu Zhang [a], Yuanyuan Lin [a], Xiaolong Wang [a], Liang Wang [c], Jing Sun [a], Tao Wang [a], Xinyan Zhang [a], Yingping Pang [a], Xiqiang Zhao [a], Yanpeng Mao [a], Zhanlong Song [a], Wenlong Wang [a], Yinghe Zhang [b], Ziliang Wang [a,*]

[a] National Engineering Laboratory for Reducing Emissions from Coal Combustion, Shandong Key Laboratory of Green Thermal Power and Carbon Reduction, Shandong University, Jinan, Shandong 250061, PR China
[b] School of Science, Harbin Institute of Technology, Shenzhen, Guangdong 518055, PR China
[c] SINTEF Energy Research, P.O. Box 4761 Torgarden, Trondheim NO-7465, Norway

ARTICLE INFO

Keywords:
Microwave discharge plasma
Methane pyrolysis
Carbon-negative Hydrogen
Carbon material
Energy saving

ABSTRACT

Methane pyrolysis is emerging as a promising carbon-negative hydrogen production technique, offering an energy-efficient alternative to conventional methane steam reforming. A novel microwave discharge plasma (MDP) system is introduced to enhance methane pyrolysis, enabling the simultaneous production of carbon-negative hydrogen and high-quality carbon materials. Key operational parameters, including microwave power, flow rate, gas composition, and reactor geometry, have been systematically investigated for their significant effects on methane pyrolysis. Optimal system performance is achieved at 300 W microwave power and a flow rate of 0.07 m/s, yielding a methane conversion rate of 99.8 % and a specific energy requirement (SER) of 180 kJ/mol, with few-layer graphene produced as a valuable byproduct. The critical role of energetic electrons, argon species, and methane interactions in C–H bond cleavage and carbon nanostructure formation is elucidated through optical emission spectroscopy (OES) analysis. Additionally, density functional theory (DFT) calculations reveal the influence of microwave fields on methane adsorption energy over tungsten surfaces, shedding light on the mechanisms of methane cracking product formation. This study provides fundamental insights into MDP methane pyrolysis, advancing sustainable methane conversion and utilization strategies.

1. Introduction

When renewable electricity or green power is coupled to chemical processes, it exhibits a striking duality. On the one hand, its zero-marginal-carbon attribute and steadily declining generation cost make it the only scalable energy vector for deep decarbonization of the chemical industry [1–3]. On the other, its intrinsic variability and anti-load profile generate a cost trilemma—curtailment, hydrogen storage, and equipment redundancy—that drives a wedge between energy utilization efficiency and economic optimality [4,5]. The "zero-carbon dividend" is real, yet so is the "variability tax": in China, inflexible chemical loads shift the abatement burden back to the grid [5]; in Europe, refusing to accept an "optimal curtailment" immediately derails green-ammonia economics [4]. Techno-economically, green power at high penetration is characterized by low marginal value, high storage dependence, and pronounced spatiotemporal coupling. The feasibility of its large-scale uptake in chemicals hinges on a calibrated trade-off between flexibility investment and curtailment tolerance. Hence, a Green Flexible Chemical Electrification (GFCE) technology—capable of millisecond-scale start-up/shut-down and distributed deployment—has emerged as the decisive enabler for overcoming green-power integration bottlenecks and achieving deep

Abbreviation: MDP, Microwave discharge plasma; DBD, Dielectric barrier discharge; MPT, Microwave plasma torch; GAP, Gliding arc plasma; OES, Optical emission spectroscopy; SER, Specific energy requirement; CAC, coal-activated carbon; HRTEM, High-resolution transmission electron microscopy; NG, Nano graphene; FWHM, Full width at half maximum; FFT, Fast Fourier Transform.

* Corresponding author.
E-mail address: zwang2022@sdu.edu.cn (Z. Wang).

https://doi.org/10.1016/j.jaap.2025.107473
Received 23 September 2025; Received in revised form 23 October 2025; Accepted 11 November 2025
Available online 14 November 2025

decarbonization [1,4,5].

Hydrogen is considered a clean energy source and a promising alternative to fossil fuels [6,7]. There are several routes for producing hydrogen, including mainly methane steam reforming, partial oxidation of hydrocarbons, methane pyrolysis, gasification of solid fuels, and electrolysis of water. However, COx production and emissions accompany these processes, except for renewable methane pyrolysis or electrolysis of water that utilizes renewable energy for power supply, which has no COx emissions [8–11].

Common methane pyrolysis technologies include thermal pyrolysis [12], catalytic decomposition [3], molten media pyrolysis [13], and plasma pyrolysis [14]. A detailed discussion of the pros and cons of those technologies is provided in Table S1. Plasma pyrolysis technology stands out due to its high conversion efficiency, low-temperature operation, high product purity, flexibility and scalability, environmental benefits, rapid reaction rates, and versatility in product applications [14]. The rapid on-off capability of plasma technology enables prompt utilization of fluctuating excess green electricity, converting otherwise curtailed electrical energy from the grid into storable chemical energy with high efficiency. It has attracted considerable attention because of its low energy consumption and high energy efficiency for its application in the direct decomposition of CH_4 [14–17]. The common plasma technologies include the dielectric barrier discharge (DBD), the gliding arc plasma (GAP), the glow discharge (GD), and the microwave plasma torch (MPT). Among the various plasma technologies [18–21], the MPT is a low-temperature nonequilibrium plasma with excellent characteristics such as higher electron density, higher ionization degree, higher particle activity, lower macroscopic temperature, and a wide range of reactor operating pressure. Therefore, it has gained the increasing attention and has been applied for such as fuel preparation [22], biomass pyrolysis [23], hazardous gas treatment [24], water treatment [25]. At the same time, microwave has been widely used in the gasification of waste plastics for value-added purposes, such as gasifying polypropylene (PP) to produce syngas and metal carbides [26], and in the decomposition of methane [14]. These applications highlight the versatility and potential of microwave plasma technology in addressing environmental and energy challenges. That non-equilibrium nature of the microwave plasma can overcome thermodynamic barriers in chemical reactions (e.g., methane pyrolysis), facilitating the reaction process and contributing to the efficient conversion of CH_4 to H_2, C, and C2 products [18,27]. Our group [28] found that it is possible to induce the generation of discharges with sharp edges, tips or sub-microscopic irregular structures in conventional microwave devices, which in turn generates discharge plasma. Researchers have utilized SiC with tip structure [29], activated carbon [22], striped metal [24,30–32] and even metal powder particles [33,34] and fluidized metal particles [35] to induce discharge in microwave field, and achieved better reaction results compared to traditional thermal conversion process. The microwave discharge generates high-energy electrons and plasma, reducing reaction activation and increasing reaction speed. Unlike MPT, this discharge excites at lower flow rates cutting costs. The microwave discharge plasma (MDP) features high electron density and energy efficiency, enabling low-energy C-H bond breaking in methane for efficient and productive cracking. In methane pyrolysis, hydrogen is the main gas product, with solid carbon as a valuable byproduct.

By retrofitting microwave sources for green-electricity operation, MDP can seamlessly satisfy the dual imperatives of millisecond-scale on/off cycling and distributed deployment demanded by renewable power, enabling the efficient valorization of otherwise curtailed electricity. Typically, microwave plasma excitation takes the form of a single-mode cavity [24,36–38]. Single-mode microwave, as a non-thermal treatment method, uses high-energy electrons to initiate methane decomposition, which reduces the required temperature and associated energy input. Single-mode microwave plasma offers the advantages of energy efficiency, fast and uniform heating, and high conversion rates [37]. At the same time, microwave devices provide fast, non-contact heating and volumetric heating that can be started up and shut down quickly, which is an advantage over conventional heating methods. However, single-mode microwave plasma devices are not cost-effective due to its dedicated design. Also for plasma torch generation, there is often a trade-off between high-power and small waveguides [22]. High-capacity microwave plasma torch generation devices are still in the research stage [39]. However, microwave plasma excitation in multimode cavities is more suitable for industrial applications because of its low cost, flexibility, and independence from cavity size [40].

This study introduces a novel MDP technique to convert methane into hydrogen and carbon materials via pyrolysis. The discharge characteristics of microwave-absorbing fillers were explored in an atmospheric pressure multimode MDP reactor. The effects of key parameters—input power, gas flow rate, gas composition, and reactor geometry—on product distribution were examined. Using OES, high-speed imaging, real-time visualization, and DFT calculations, the study elucidated reaction intermediates and plasma properties. This work identifies optimal conditions for enhancing reaction efficiency and selectivity, providing insights into methane pyrolysis mechanisms and advancing sustainable energy solutions.

2. Results and discussion

2.1. Discharge characteristics of SiC and CAC

The microwave field caused many hot spots in the filler bed, which was a microwave discharge phenomenon triggered by the microwave electromagnetic field. Driven by the microwave field, electrons are free to move and accumulate at places of high curvature such as tips, burrs, crack edges, and pore edges on the material surface. The charge density on the curved surface of the material can be thousands of times greater than the rest of the material [22]. Studies by others have shown that [22,24,28,29], the greater the surface curvature, the higher the surface charge density and the greater the potential difference between the fillers.

The very high potential difference creates a high-voltage electric field that increases the kinetic energy of some free electrons, driving them to hit gas molecules at high speeds in inelastic collisions. This leads to the formation of positive ions and more secondary electrons and an “avalanche effect” that produces a large amount of plasma [28]. Excited states of matter in a plasma, such as Ar in the excited state, and positive and negative ions with an electrical charge. When collisions and recombination occur, excess energy is released in the form of photons and heat, which manifests itself on the macroscopic scale as visible electrical sparks [22,29].

The discharge characteristics are related to the material used for the discharge. Under the same operating conditions, the discharge characteristics of different materials can vary greatly. Better wave-absorbing properties will make it easier to generate a discharge. Three microwave-absorbing materials (foam SiC, CAC, and tungsten needle) were chose to study MDP phenomena and their characteristics. Through the investigation of two parameters, namely the filler and bed height, the tungsten needle has been selected for further optimization based on performance criteria such as methane conversion rate. The corresponding results are presented in Fig. S2.

2.2. Characteristics of MDP induced by tungsten needle

Preliminary tests found the tungsten needle could generate a strong plasma in the microwave field. Therefore, a comprehensive study of effects of key parameters on the MDP was conducted.

The effect of power on the MDP characteristics of tungsten needles was firstly investigated, as shown in Fig. 1(a), (c), and (e). When the microwave output power was 200 W, there was basically no arc through the screen plate. As the power increased from 200 W to 300 W, the observation was changed from no arc to intermittent arc through the

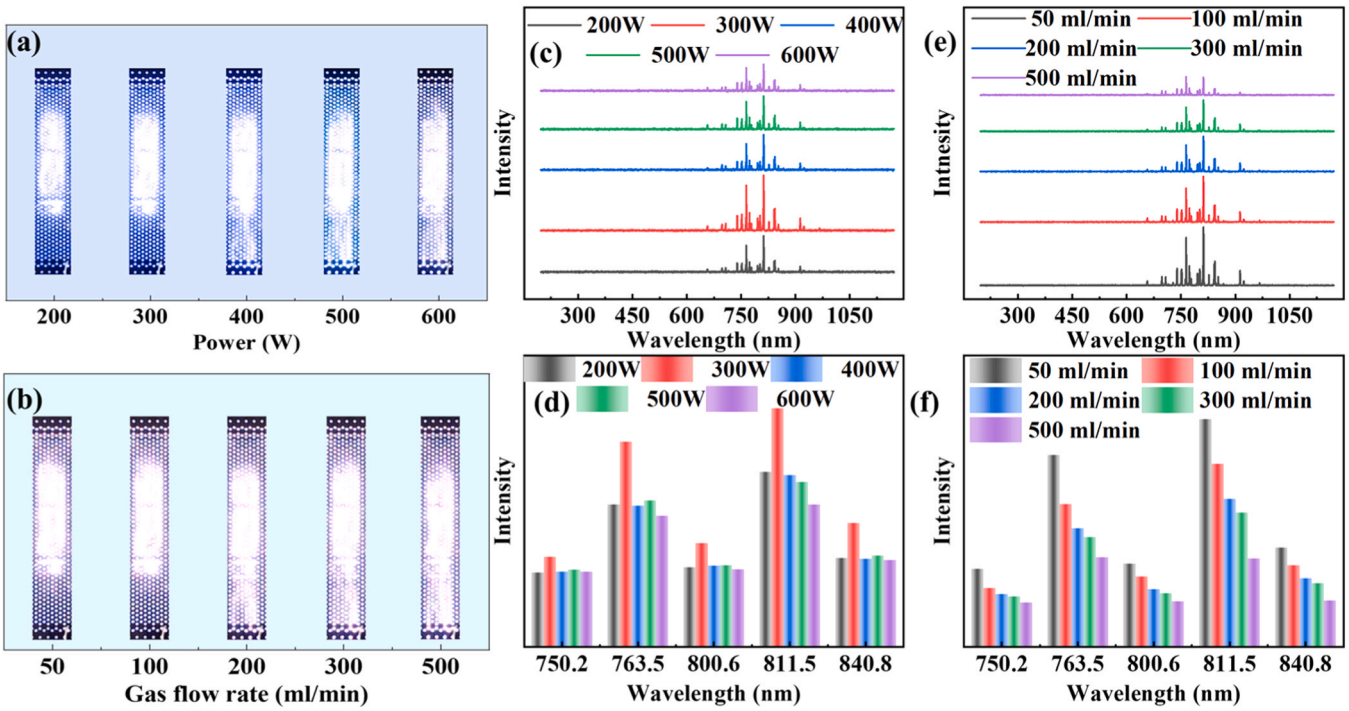

Fig. 1. Discharge characteristics of different fillers. (a) and (b) Discharge images of tungsten needles in pure Ar atmosphere under different conditions;(c) -(f) Spectral intensity of tungsten needles discharged under different conditions in pure Ar atmosphere.

screen plate. When the power reached more than 400 W, the arc was long enough to penetrate the screen plate. That is because with increasing of power, the enhanced energy input intensifies the discharge, leading to a more robust arc and a progressively expanding discharge area.

As shown in Fig. 1(b), (d), and (f), the influence of Ar flow rate parameters on the MDP characteristics of tungsten needles was examined. At 300 W and 100 ml/min, the penetration of the screen plate occurred only sporadically. However, when the Ar flow rate increased to 200 ml/min, this penetration became a consistent phenomenon, indicating that the enhanced gas flow facilitates the transport of the arc through the screen plate. Notably, while a higher flow rate generates a larger arc, it simultaneously suppresses the vertical extension of the arc, resulting in a reduction in the height of the discharge region. Another potential reason for the reduced height of the discharge region is reactor design issues. The current direction of the airflow is top-down, which results in the arc being carried by the airflow, providing a guiding direction for future reactor optimization.

The microwave Ar discharge plasma was further characterized using the optical emission spectroscopy (OES) [41], as depicted in Fig. 1(c)-(f). Fig. 1(c) and (e) present the full spectra of Ar plasma under different conditions. The characteristic emission lines of Ar are distinctly visible, further validating the excitation of Ar in the plasma [42]. Fig. 1(d) and (f) display the emission intensities at characteristic wavelengths of Ar, including 750.2 nm, 763.5 nm, 800.6 nm, 811.5 nm, and 840.8 nm, under varying experimental conditions. The significantly high emission

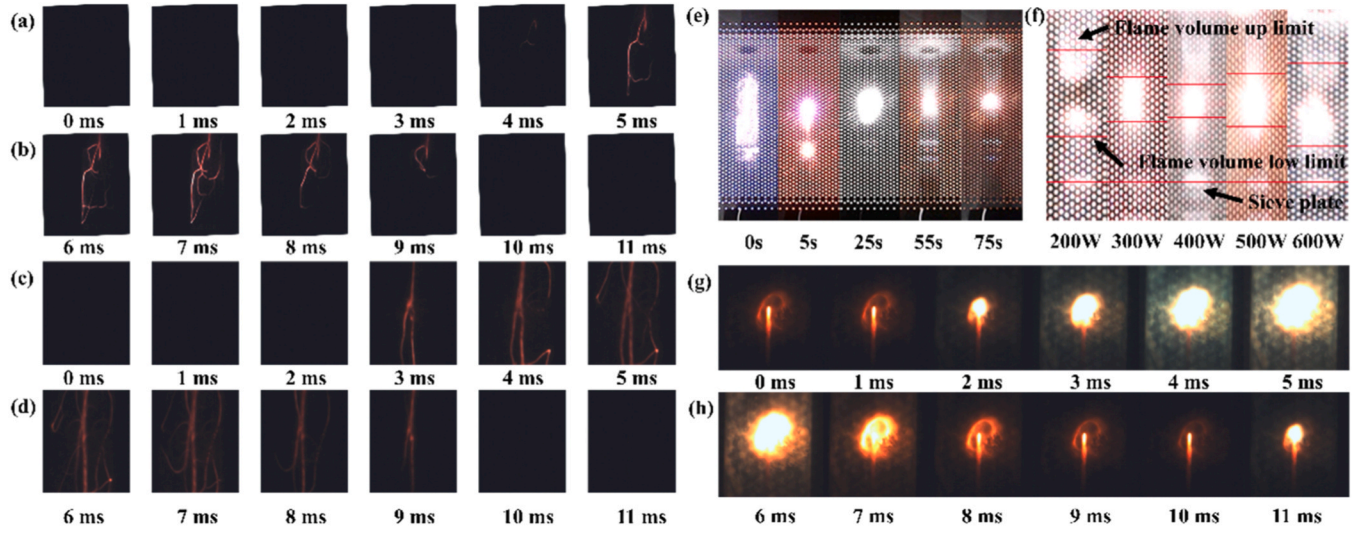

Fig. 2. Images of pure Ar and 10 %methane discharge. (a) –(d) Ar discharge picture of 300 W, 100 ml/min pure Ar at 1 ms per image((a) and (b) at 4800FPS, (c) and (d) at 9000FPS); (e)Evolution of MDP states after methane pass-through; (f) Characterization of methane plasma flames at different powers. (g) and (h) 0–5 ms and 6–11 ms discharge images at 9000 FPS with 300 W, 100 ml/min discharges, respectively.

intensities at these wavelengths confirm the effective excitation of Ar. From Fig. 1(c), it is evident that increasing power initially suppresses Ar discharge. Fig. 1(f) reveals that the emission intensities at all wavelengths are the highest at a flow rate of 50 ml/min Ar. The overall trend demonstrates that higher flow rates promote arc expansion while simultaneously restricting its vertical extension, which is consistent with the observations in Fig. 1(b).

The excitation process of Ar discharge plasma was also captured by a high-speed camera, as illustrated in Fig. 2(a)-(d). At frame rates of 4800 and 9000 FPS, the discharge cycle was observed to be approximately 10 ms, with an excitation time of 3.5–3.6 ms and a discharge duration of 6.7–7 ms. Despite slight differences of frame rate and image resolution, the consistency in discharge cycle duration across both frame rates validates the temporal parameters of the discharge process.

2.3. Key parameters in microwave plasma discharge for methane pyrolysis using a Tungsten needle

The discharge feature of a tungsten needle is significantly different from that of the activated carbon. With presence of Ar, the tungsten needle, owing to its pronounced surface curvature at the tip, generates a potent tip discharge, leading to a distinct and intense arc discharge that manifests as a vivid blue-violet arc. However, when methane is introduced into the reaction zone, the arc dynamics shift due to methane's inherent properties that inhibit gas discharge. Methane first produces a flame-like discharge at the tip of the needle. At the same time, a discharge occurs between the two sieve plates, but it quickly subsides. The flame-like discharge develops gradually with the continuous inflow of methane gas until it is completely stabilized. Contrary to the pronounced arc observed with Ar, methane induces a more subdued filamentary discharge. This results in the formation of a flame-like, high-energy region at the needle's tip, which is pivotal for the ensuing reactions.

Fig. 2(e) illustrates the impact of methane introduction on the discharge characteristics. Initially, when methane is introduced, the original purple Ar arc transitions into a mixed discharge displaying both purple and red hues. As the methane inflow duration increases, the white methane discharge gradually becomes dominant. Upon stabilization of the methane discharge, a needle-tip flame is formed, exhibiting a distinct red color. Fig. 2(f) depicts the variation in methane flame volume with different powers. The flame volume follows a parabolic trend, initially decreasing and then increasing with rising power.

As shown in Fig. 2(g) and (h), the high-speed camera, operating at a frame rate of 9000 FPS, captures the evolution of tungsten needle-induced microwave discharge methane plasma. The introduction of methane significantly alters the discharge behavior. Unlike the intermittent discharge observed in pure Ar, the addition of methane results in a more continuous, flame-like filamentary discharge. In this case, the subsequent discharge cycle initiates before the previous one fully dissipates. The extremely high energy generated causes the tungsten tip to glow red, indicating an exceptionally high temperature at the tip. Similar to Ar, the methane discharge cycle spans approximately 90 frames, equivalent to 10 ms. The discharge reaches its fullest form in about 4 ms, then gradually diminishes, with the flame-like production lasting approximately 6 ms.

Nevertheless, under identical conditions, the tungsten needle exhibits a pronounced enhancement in reactivity, which is attributed to the intense discharge. As shown in Fig. S2(a), this vigorous discharge has been instrumental in achieving a methane conversion rate as high as 98 %. Due to space constraints, when the height of the tungsten needle tip is located above and below the height of the waveguide, the position of the arc spark exceeds the up and low limits of the microwave reactor cavity. Therefore, tungsten needles are not involved in the tip position discussion. This section focuses on the effects of power, flow rate, gas ratio, and reactor size on the methane conversion process.

2.3.1. Microwave power

The Fig. 3 shows the effect of microwave power on the methane pyrolysis reaction. With introduction of 100 ml/min of mixture of 10 vol % methane and 90 vol% Ar, the best conversion of methane reached more than 98 % at 200 W, the best H_2 selectivity was more than 65 % at 600 W, and the best C2 selectivity reached 48 % at 200 W. Due to the intensive of tungsten needle discharge, the plasma generated at multiple discharge points strongly promoted the methane pyrolysis reaction.

The experimental results revealed that as the microwave power increased from 200 W to 600 W, as shown in Fig. 3(a), the conversion rate of methane decreased from 98.04 % to 95.35 % and then increased to 97.56 %. This change was not significant, potentially attributed to the excessive ionization of the plasma caused by the higher power. The increased electron density resulting from excessive ionization may have caused the plasma to contract, thereby reducing the residence time of the reactants within the plasma region [43]. However, the higher power would bring more active particles and electrons, which in turn led to a higher reactivity at shorter residence time, realizing a rebound in the conversion rate. It is noted that, higher power can generate particles with elevated kinetic energy, inducing more violent and frequent collisions of particles. This enhanced collisional dynamics promotes complex reaction pathways, which are subsequently followed by electron collision-mediated dissociation processes [44]. Therefore, higher power results in more energy to achieve higher methane pyrolysis efficiencies, which ultimately results in higher hydrogen production rates at higher power. However, it is found that the hydrogen production is quite low at 400 W. One of the reasons may be that the higher power will over-ionize the plasma and lead to a lower chance of H_2 production, which is consisted with the lowest flame volume of 400 W shown in Fig. 2(f).

Based on reaction equations of methane pyrolysis, the generation of C2 products tends to be inversely proportional to hydrogen generation, namely the more hydrogen produced, the less C2 is produced. At the start of the reaction, the high-energy electron density is elevated, making it easier to break C–H bonds and form solid carbon and hydrogen. As the concentration of free radicals increases, they begin to influence the reaction alongside the high-energy electrons, affecting the production of solid carbon and hydrogen. Thus, under stabilized reaction conditions and in correlation with the reaction parameters, the selectivity of both solid carbon and C_2H_6 reaches approximately 50 %, respectively. As shown in Fig. 3(a) and (c), it is obvious that the higher energy leads to the preferential formation of solid C and hydrogen in the reactor, with very limited formation of C_3 and C_4. It is further found that C_2H_6 is the dominant one of C2 products as shown in Fig. 3(d). It has been reported C_2H_6 is often the most readily formed product in the C2 products, followed by C_2H_4, and then C_2H_2 considering conversion of methane. The selectivity of C_2H_6 is not strongly dependent on microwave power, which is due to the fact that the reaction volume of methane in the current 18 mm diameter reactor is too large to be fully reacted at the current microwave energy. Also, the C-C bond is much easier to bind than the C-H bond to break, so the methyl radical prefers to couple to produce C_2H_6. C_2H_4 is produced mainly by ethane dehydrogenation and radical collisions, and C_2H_2 is further dehydrogenated.

The ideal value of SER depends on the power and flow rate. Fig. 3(b) presents that the value of SER increases as the power increases from 120 kJ/mol to 360 kJ/mol. Given that power augmentation exerts negligible influence on methane conversion efficiency, the SER of methane is in strict agreement with the ideal SER curve, rising from 122 kJ/mol to 369 kJ/mol with parametric variation [24]. Since substantial C2 by-products generation as shown in Fig. 3(c), the SER of hydrogen is far from the ideal curve, increasing from 231 kJ/mol to 558 kJ/mol with increasing power.

2.3.2. Flow rate

Fig. 4(a) shows the total flow rate was increased from 50 ml/min to 500 ml/ min, the conversion of methane decreased from 98.29 % to 82.19 % and then rose to 89.68 %. It is attributed to the fact that the

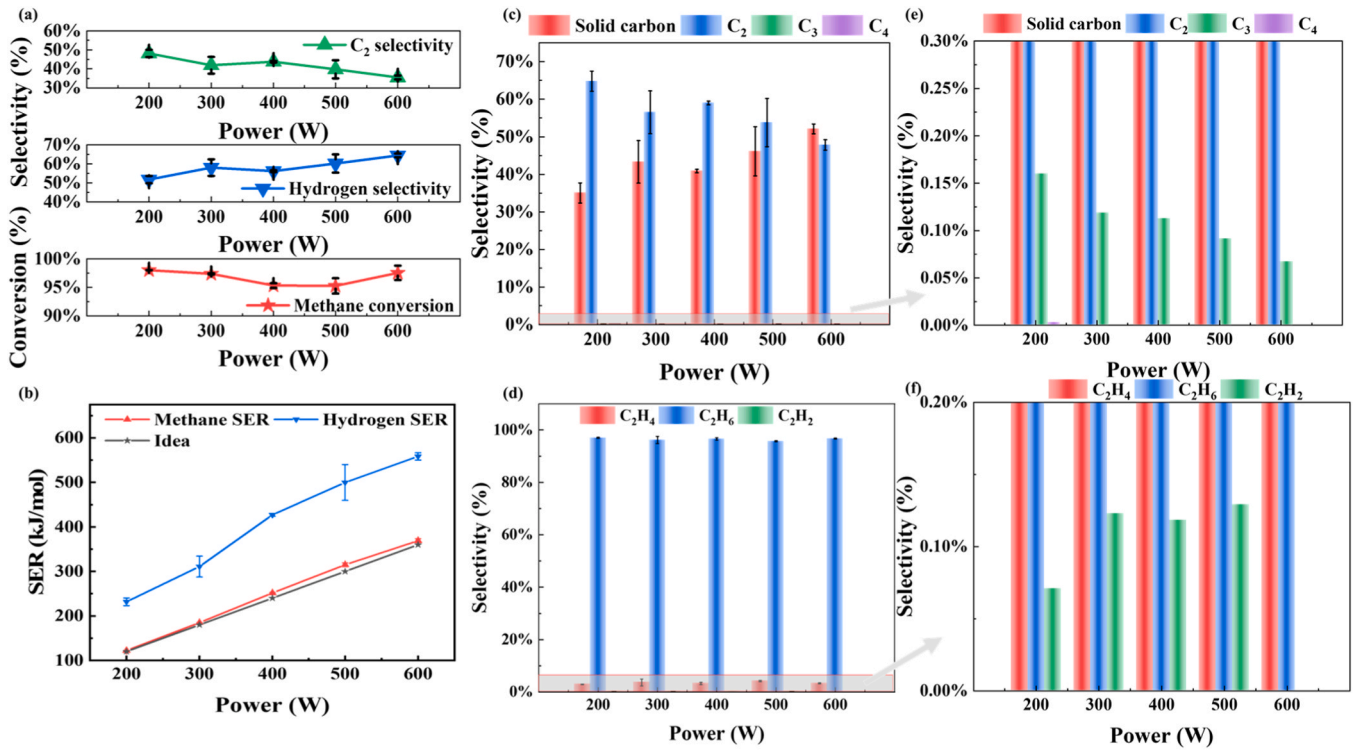

Fig. 3. Performance of the MDP system for methane conversion in diffirent power. (a) Methane conversion, hydrogen selectivity and C2 selectivity; (b) SER (Note: The term "idea" is considered to represent the scenario where methane undergoes complete reaction under the current conditions, such as power and flow rates.); (c) and (e) C product selectivity; (d) and (f) C2 product selectivity.

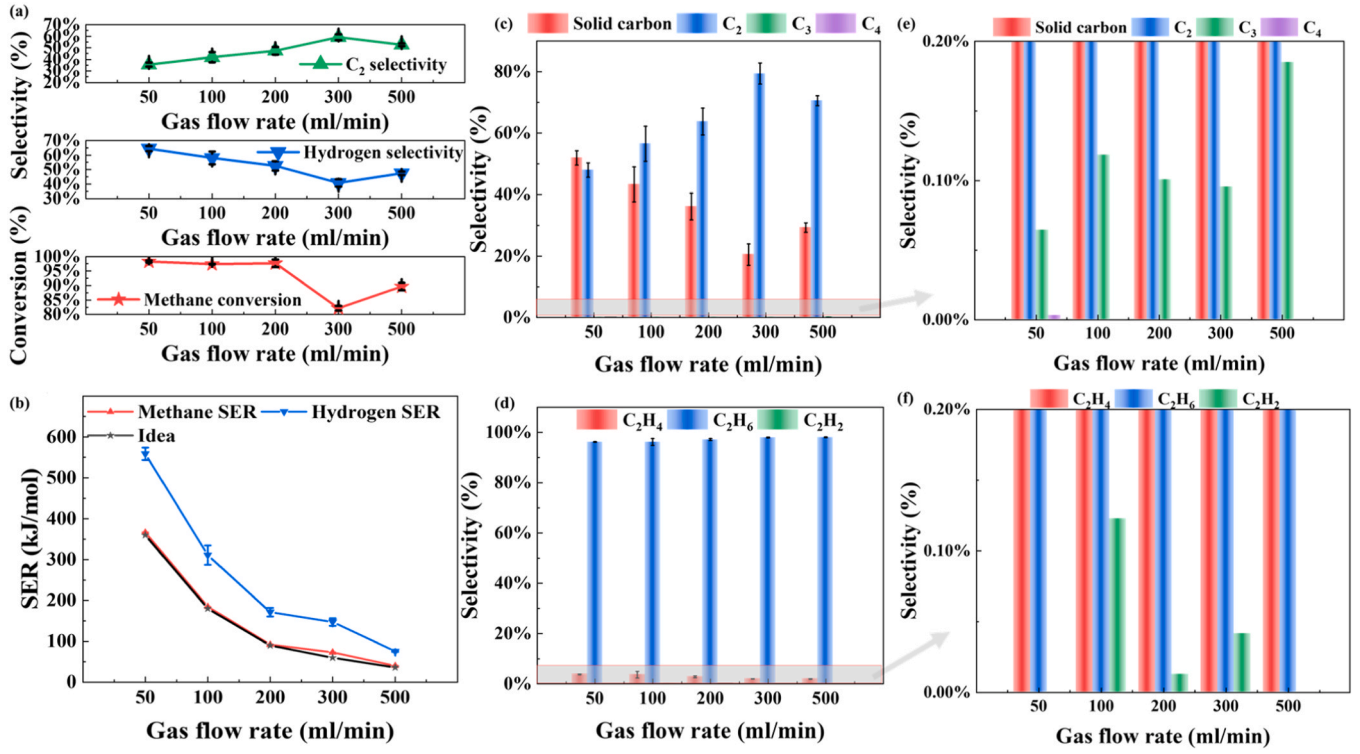

Fig. 4. Performance of the MDP system for methane conversion in diffirent gas flow rate. (a) Methane conversion, hydrogen selectivity and C2 selectivity; (b) SER; (c) and (e) C product selectivity; (d) and (f) C2 product selectivity.

increase in the flow rate had a negligible effect on the plasma volume, which merely reduced the residence time of CH_4 [24]. However, the presence of the porous plate at the bottom of the reactor can potentially affect the flow rate of the gas. As the pass through the porous plate, gas might a higher flow velocity as it across the plate's holes, leading the perturbation of the pinpoint flame. This caused disguise of the increase

of the reaction area and made the conversion rate increase instead of decrease.

As shown in Fig. 4(a), the higher flow rate reduces the chance of energetic particle collisions. This observation is probably related to the hydrogen selectivity, which decreases first and then increases with the flow rate, consistent with methane conversion. Higher flow rates increase the probability of collision of free radicals (e.g., CH_3·, etc.) and heavy particles (Ar), leading to higher C2 selectivity and a decrease in the selectivity of solid C, and also a near absence of C_3 and C_4 production, as shown in Fig. 4(c). This is the opposite of the conversion rate trend as shown in Fig. 4(a). Fig. 4(d) shows the dominance of C_2H_6 in the C2 products, which is similar as varying the power parameter. Higher flow rates result in less reaction time of the methane, which significantly limits collision reactions of free radicals. Less residence time can reduce collisions between radicals and electrons, making reactions such as C-H bond breaking more difficult to occur. One the other hand, this also leads to higher C_2H_6 selectivity. It is thought that the coupling of radicals is much easier. However, the higher flow rate carries a small amount of C out of the reactor and reduces the amount of C attached to the inner wall of the quartz tube used. This indicates that carbon from the reaction is deposited on the tube wall. When the flow rate is too high, the carbon does not have time to be deposited on the wall of the tube before it moves on to the next region with the gas flow.

Fig. 4(b) shows that the SER decreases with an increase of flow rate from 360 kJ/mol for 50 ml/min to 36 kJ/mol for 500 ml/min. The SER of methane decreases from 366 kJ/mol to 40 kJ/mol with increasing flow rate. Notably, while methane conversion exhibits a zigzag pattern, methane SER shows a monotonous decline. Hydrogen SER deviates significantly from the ideal curve, dropping from 558 kJ/mol to 75 kJ/mol with flow acceleration, as direct conversion of 1 mol methane to 2 mol hydrogen is not fully realized during the reaction.

2.3.3. *Ratio of CH_4 and Ar*

During the MDP process, the composition of methane significantly affects the pyrolysis efficiency and product distribution [14]. The impact of different volumetric fractions of Ar on the reaction has mainly been discussed. Preliminary tests found that an excessively high molar fraction of methane in the mixture of methane and Ar resulted in plasma quenching. This observation underscored the pivotal role of Ar in plasma excitation. Consequently, discussions of reactions and conversion behaviors of the methane in this section focusing on these took place under conditions where the CH_4:Ar molar ratio does not exceed 5:5.

Fig. 5(a) shows that as the CH_4:Ar ratio increased from 1:9–5:5, the methane conversion rate correspondingly rose from 97.32 % to 98.66 %. Both Ar molecules and high-energy electrons critically affect conversion of methane. The energetic electrons induce direct cleavage of methane's C-H bonds via electron impact, generating carbon deposits and hydrogen species. Increased methane concentration enhances electron-molecule collision frequency, thereby producing a proportional enhancement in conversion efficiency with rising CH_4:Ar ratios [45].

As shown in Fig. 5(a), it is observed that as the CH_4:Ar increases from 1:9–3:7, the selectivity of hydrogen and solid carbon decreased. This can be attributed to the inhibition of pinpoint flame formation by the increased presence of methane. The additional methane was insufficient to compensate for the reduced flame volume, leading to a decrease in hydrogen selectivity and an increase in selectivity of C2. When the ratio reached 5:5, however, the increased amount of methane had a chance to interact with the pinpoint flame, compensating for the diminished flame volume and resulting in a rebound in hydrogen selectivity.

Fig. 5(c) and (d) show that the distribution C products and C2 products, respectively. Fig. 5(c) shows that the products are still mainly solid carbon and C2, and the change in formation of solid carbon is in line with the change in hydrogen selectivity. Fig. 5(d) shows the dominance of C_2H_6 in the products, which are both greater than 93 %. More methane content brings more chances for radical collisions, but the weakening of the discharge strength by the reduction of argon molecules also leads to a reduction in the number of high-energy electrons, so that both the selectivity of the C2 product and the selectivity of ethane show a parabolic trend of increasing and then decreasing, and reach a

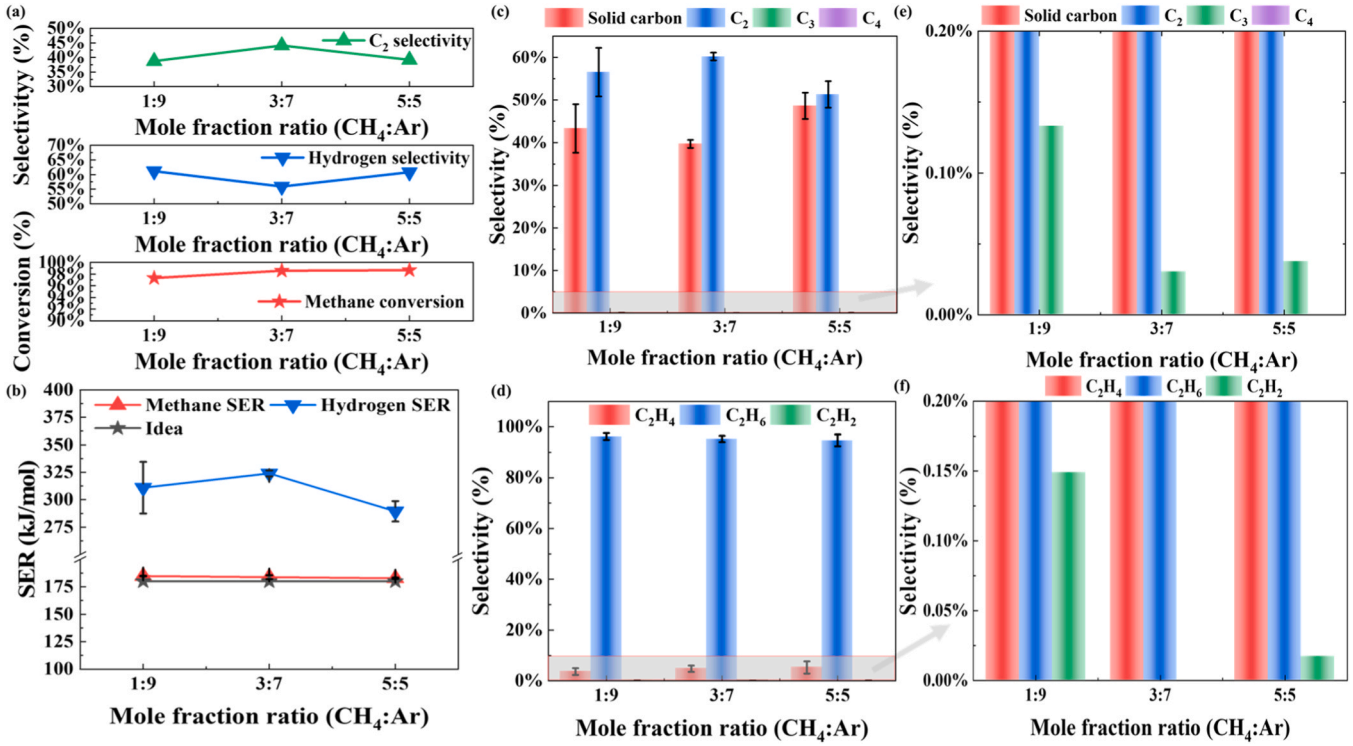

Fig. 5. Performance of the MDP system for methane conversion in different mole ratio. (a) Methane conversion, hydrogen selectivity and C2 selectivity; (b) SER; (c) and (e) C product selectivity; (d) and (f) C2 product selectivity.

maximum at 3:7. Fig. 5(b) shows that with no change to the flow and power, the ideal SER does not change and is equal to 180 kJ/mol. As the CH_4:Ar molar ratio becomes larger, the SER of methane decreases from 185 kJ/mol to 183 kJ/mol and finally to 182 kJ/mol. The trend in SER is related to the trend in the corresponding conversion rate. Since the hydrogen selectivity changes significantly, the SER changes significantly while deviating from the optimal curve, rising from 187 kJ/mol to 215 kJ/mol before falling back to 189 kJ/mol as the CH_4:Ar molar ratio

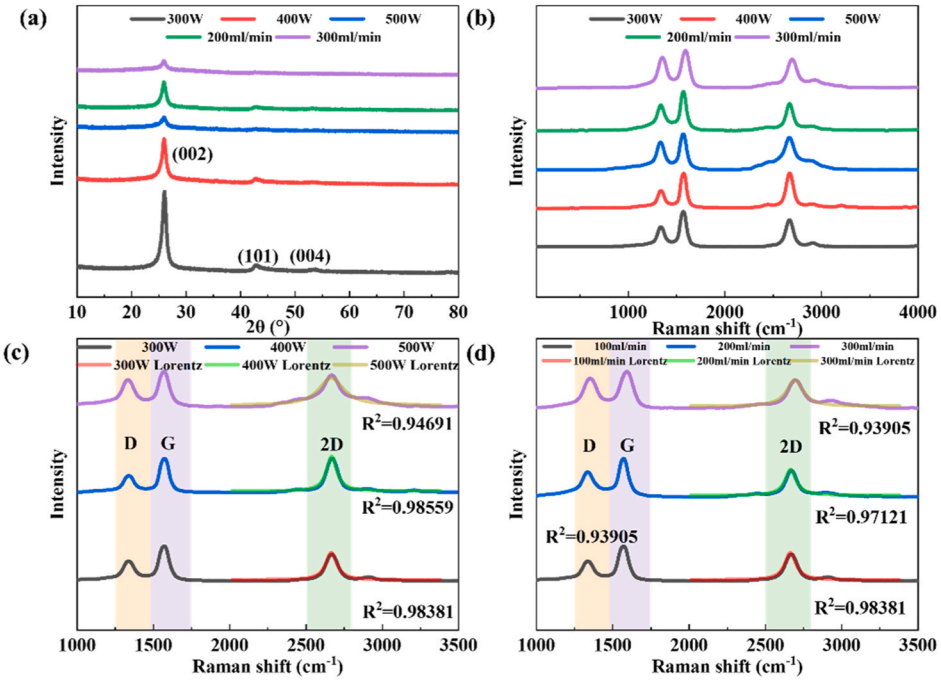

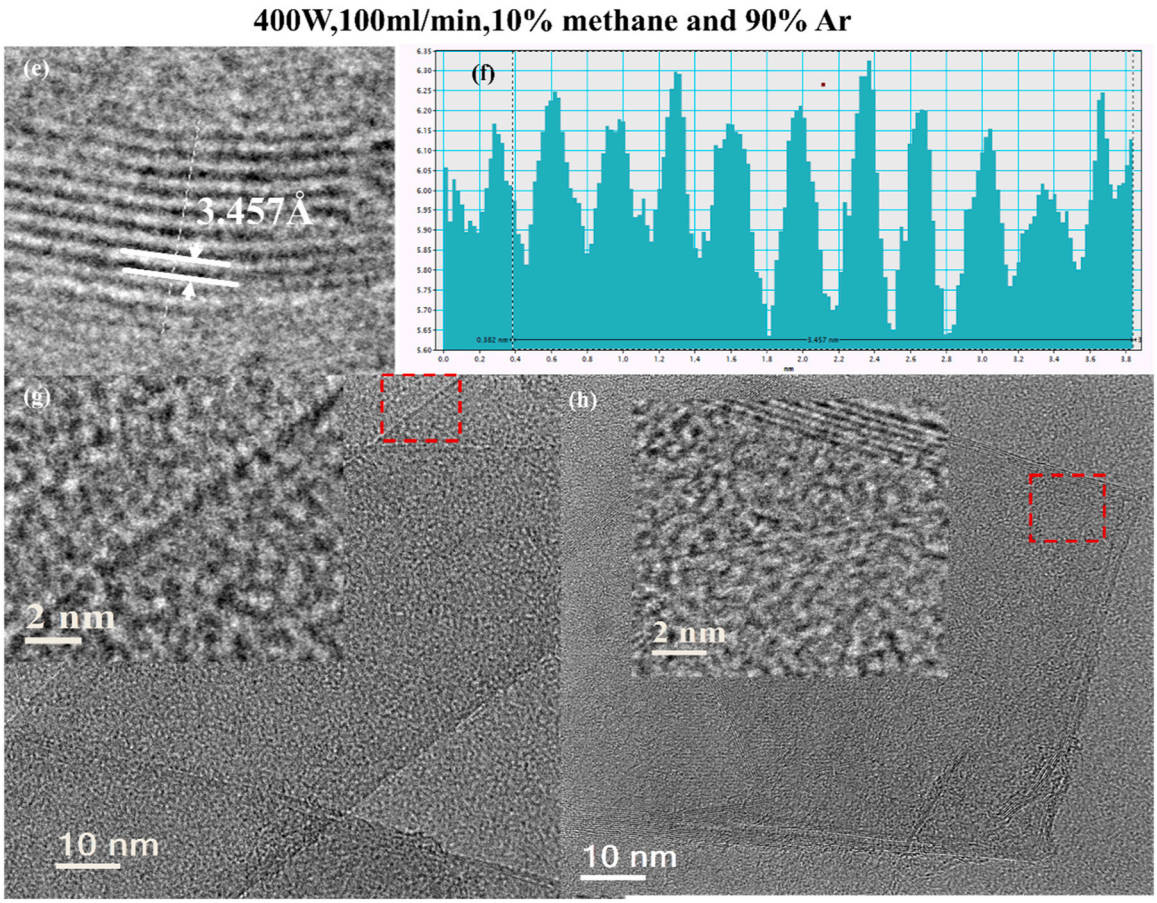

Fig. 6. Condition-dependent carbon product structure evolution with 10 % methane and 90 % Ar mixture. (a) XRD and (b)-(d) Raman spectral images under different conditions; (e) selected area zoomed in, (f) Graphene layer spacing, (g) and (h) Few-layer graphene.

becomes larger.

2.3.4. Needle diameter to reactor inner diameter ratio

To investigate the influence of the geometrical parameters of the reaction zone, especially the reactor diameter, on the reaction performance, one parameter is defined as the needle diameter to reactor inner diameter ratio. That is a dimensionless parameter to represent

the difference between the needle size and the reactor size. A larger diameter ratio means a smaller reaction area. In this study, the largest reactor diameter is 5 times of the smallest one. As shown in Fig. S3(a), a higher methane conversion rate, close to 100 %, can be achieved by using a smaller reactor. Whereas it was found that changes in diameter ratio had slight effects on the methane conversion, indicating the reactor used in this work designed well with a high methane conversion efficiency. At conditions of 300 W, the superficial gas velocity for all cases was 0.07 m/s. Methane was converted primarily to solid carbon (C) and hydrogen, with hydrogen selectivity approaching 100 % and negligible C2 production. This was attributed to the increased contact between methane and the pinpoint flame in a larger diameter ratio, which allowed the high-energy electrons to interact directly with the C-H bonds, thus facilitating direct pyrolysis.

Effect of the diameter ratio on the SER is shown in Fig. S2(b). The ideal SER will be higher for a larger diameter ratio because the reaction region with a larger diameter ratio requires a reduced volumetric flow rate to maintain the same apparent gas velocity. Therefore, larger reactors may be less favorable in terms of energy efficiency. Due to the very high methane conversion and hydrogen selectivity, the experimental curves of SER almost coincidentally match with the ideal curve. As the diameter ratio becomes smaller from 0.25 to 0.056, the SERs of methane and hydrogen change from 3000 kJ/mol to 180 kJ/mol.

2.4. Carbon products

2.4.1. X-ray diffraction of plasma carbon

The composition of the five carbon products was analyzed by XRD, and the XRD spectra of all the samples are shown in Fig. 6(a). The XRD analysis of the carbon products at 300 W, 100 ml/min, 90 % Ar and 10 % methane showed a sharp 002 peak accompanied by 101 and 004 peaks. Meanwhile, with the constant power of 300 W, as the flow rate increases from 100 ml/min to 200 ml/min, the intensity of peak 002 decreases, but the peak itself retains a sharp shape. The intensity of peak 101 shows minor change, while peak 004 has almost disappeared. When the flow rate is increased to 300 ml/min, the intensity of peak 002 decreases dramatically with increase of peak width and peaks 101 and 004can not be identified. Meanwhile, with the flow rate kept constant at 100 ml/min, the intensity of peak 002 decreased slightly as the power was increased from 300 W to 400 W, while the peak itself retained sharp. The intensity of peak 101 remained nearly unchanged, whereas peak 004 had almost disappeared. When the power was further increased from 400 W to 500 W, the intensity of peak 002 decreased dramatically. No peak 101 and 004 can be detected. Since XRD is a spatial averaging technique that probes milligram-scale sample volumes, the obtained spectra are representative of the bulk material when the sample is homogenously mixed. The crystallographic spacing (D-spacing) was calculated using Bragg's law based on the full width at half maximum (FWHM) of the peak at $2\theta = 26.5^{\circ}$ as shown in Table 1. The determined graphite interlayer spacing of approximately 3.42 Å shows only minor deviation from the ideal graphite crystal value (3.35 Å). Notably, the D-spacing exhibits a gradual expansion from 3.420 Å to 3.432 Å with increasing power, and a similar trend is observed with increasing flow rate (3.420 Å to 3.432 Å).

Table 1
XRD FWHM, d002 and Raman peak ratio.

Sample (10 % methane and 90 % Ar)	FWHM/ degree	d002/ Å	ID/ IG	IG/ I2D
300 ml/min,300 W	0.682	3.432	0.823	1.303
200 ml/min,300 W	0.719	3.432	0.669	1.415
100 ml/min,300 W	0.687	3.420	0.586	1.285
100 ml/min,400 W	0.687	3.424	0.528	0.996
100 ml/min,500 W	0.761	3.432	0.781	1.134

2.4.2. Raman of plasma carbon

The I_D/I_G peak ratios and plots of the Raman spectra for the five samples are depicted in Fig. 6(b)-(d) and Table 1. As shown in Fig. 6(b), the presence of D peaks in all five samples indicates the presence of amorphous carbon within the carbon material. Meanwhile, the broader 2D peaks suggest the potential presence of multilayered graphene, albeit with a small number of layers. As shown in Table 1, the I_D/I_G peak ratios for all five samples are below 0.9, signifying a high degree of graphitization in the carbon material. I_D/I_G decreases and then increases with increasing power and increases with increasing flow rate. Notably, the peak I_D/I_G ratio approaches 0.5 at 400 W and 100 ml/min, reaching 0.528. Table 1 shows no clear trend in the I_G/I_{2D} ratio, except at a flow rate of 200 ml/min, where it slightly exceeds 1.40 (reaching 1.41). The other four values remain below 1.4. Notably, at 400 W, the ratio drops to 0.996. A higher number of graphene layers induces a redshift in the 2D peak wavelength. Monolayer graphene exhibits a perfect Lorentzian single peak are shown in Fig. 6(c) and (d) [46]. The fitting quality aligns with XRD results but slightly degrades with increasing power and flow rate. However, the carbon product synthesized at 400 W and 100 ml/min demonstrates the best peak fitting and quality, consistent with the optimal peak ratio. This also accounts for the fact that it has a few-layer graphene structure.

2.4.3. HRTEM of plasma carbon

The high-resolution transmission electron microscopy (HRTEM) images of the samples at different resolutions are presented in Fig. S6. Fig. S6(a) captures the morphological features of the carbon material at low resolution. From the Fig. S6(a) scanned sample with distinct structural differences can be seen, which are related to presence of amorphous carbon, graphite, and graphene. The scanned regions exhibit a disordered arrangement indicate presence of amorphous carbon, while the graphite domains display a more ordered, layered structure. In Fig. S6(b), a more detailed and well-defined multilayer graphene structure is visualized, facilitated by the relative offset of the layers, which enhances the contrast and clarity of the individual graphene sheets. The formation of graphene folds, a common feature in multilayer graphene systems, is also prominently observed. These folds arise due to the mechanical stress and strain during the synthesis process, leading to the bending and stacking of graphene layers [47,48]. The observations reveal that the majority of the graphene layers consist of 2–6 layers, indicating a controlled and relatively uniform growth process. The presence of few-layer graphene, particularly single and bilayer graphene, was further confirmed through these observations, as illustrated in Fig. 6(f) and (g). The few-layer graphene structure, highlighted within the red circle, aligns with the findings from Raman spectroscopy, which typically shows characteristic peaks such as the 2D band and G band that are sensitive to the number of layers. The consistency between HRTEM and Raman results underscores the reliability of the structural characterization.

To further analyze the properties of the samples and gain deeper insights into their

crystallographic features, Fast Fourier Transform (FFT) analysis was conducted, as shown in Fig. S7. Graphene boundaries with thicker layers were selected to determine the lattice spacing parameters of the scanned sample more accurately. By drawing a plumb line perpendicular to the graphene layer structure, the peak intensity and layer spacing for each layer were obtained, as shown in Fig. 6(e)and(f). The lattice spacing, calculated by averaging ten selected peaks, was determined to be 3.457 Å, which is in well agreement with the 3.35 Å theoretical

interlayer spacing of graphene. This slight deviation could be attributed to the presence of defects, functional groups, or residual strain within the graphene layers. In addition to HRTEM, SEM and conventional TEM were also provided, as shown in Fig. S4 and Fig. S5.

2.5. Mechanism of MDP reaction excited by tungsten needles

2.5.1. OES measurements

For the CH_4-Ar plasma cases with a CH_4 concentration of 10 %, the intensity of the spectral lines corresponding to CH_4 and Ar transitions increases with rising microwave power, as shown in Fig. S8. This indicates that the microwave power can affect the ionization process within the plasma. In addition, the spectral peaks show different changes with the increase of microwave power. The intensities of the C II spectral line and the Swan band are significantly highest at 200 W, while the intensity of the C-H peak is also higher than that at 600 W. This is consistent to the conversion rate. The effect of the variation of flow rate on the spectra is also shown in Fig. S8. Unlike the power variation, the overall spectral intensity is slightly higher for 100 ml/min than for 50 ml/min, but the trend is the same.

The detected atomic emission spectra and atomic lepton spectra confirm that MDP can achieve molecular decomposition of CH_4 through high-energy electron collisions, with many electronically excited atoms playing a significant role in the CH_4 transformation process. The microwave discharge generates a substantial amount of excited CH_4* involved in the reaction. Note that hereafter an asterisk (*) denotes an excited state (e.g., A* represents species A in an excited state). When the energy of electron collisions exceeds the bond energy of the C-H bond, CH_4 undergoes electron collisional dissociation, leading to the formation of CH_x· (x = 1, 2, 3) and hydrogen atoms. As shown in Fig. S8 the peaks of C and C-H appear in the microwave discharge spectrum of the tungsten needle. It indicates that the discharge excites CH_4, which is then dissociated by electron collisions to produce CH_x· and promotes the reaction. Concurrently, Ar, as a heavy particle, also facilitates electron collisions into the Ar molecule, leading to the excited state Ar*, which carries the energy of the electrons. The collision of Ar* also transfers

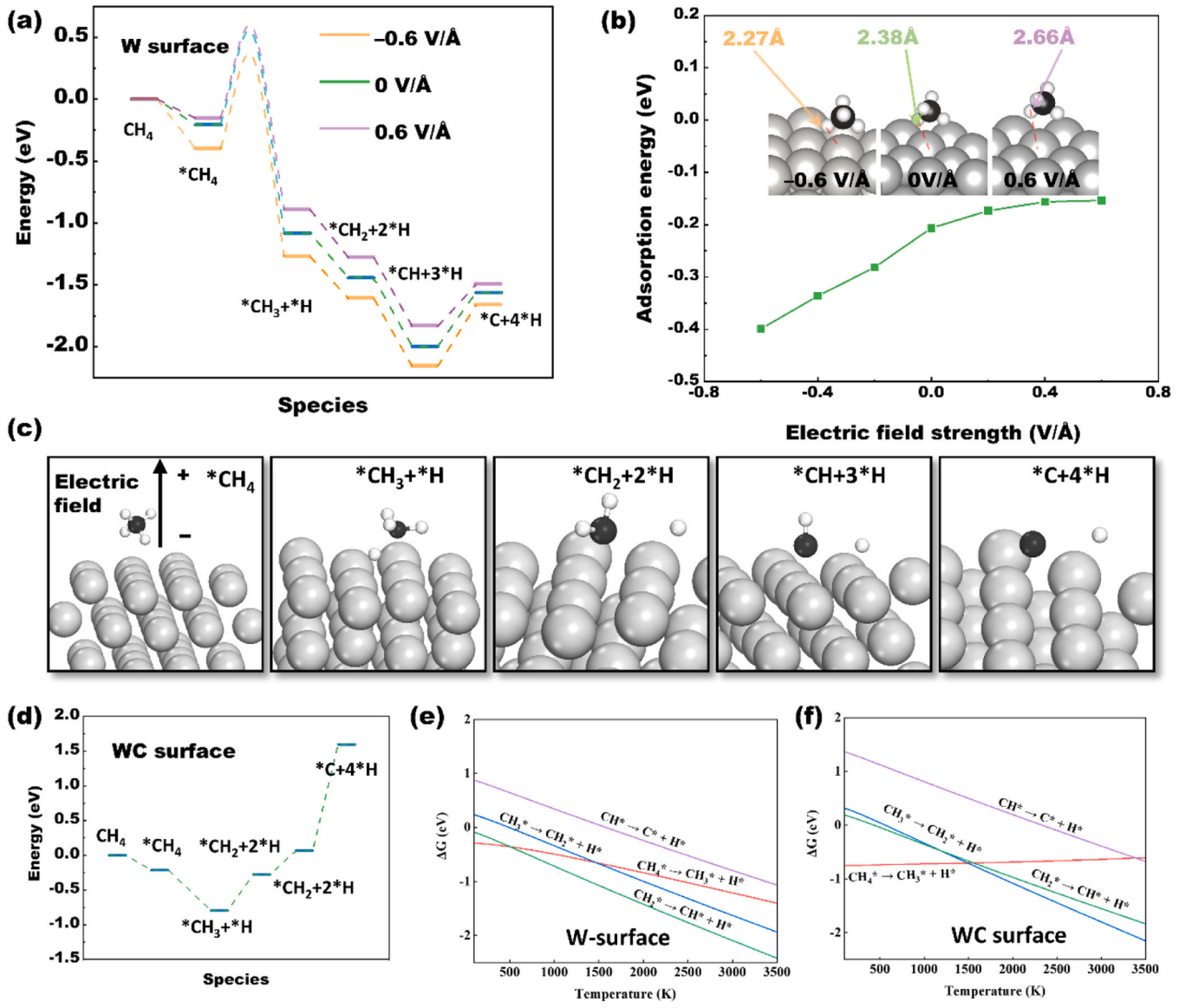

Fig. 7. Effect of microwave-induced electric fields on methane dissociation over a tungsten metal surface: (a) Influence of electric fields on adsorption energies during dissociation steps; (b) Evolution of methane adsorption distance under varying electric fields; (c) Detailed dissociation pathway of methane on the tungsten surface; (d) energy change of methane dissociation reactions on WC surface (W-termination); (e) T-ΔG (Free energy change) for methane dissociation reactions on tungsten (W) surface; (f) T-ΔG (Free energy change) for methane dissociation reactions on WC surface (W-termination);.

energy, resulting in the breakage of the C-H bond. The Ar II peak is present in the microwave discharge spectrum of the tungsten needle. It indicates that the discharge excites Ar, and electron collision generates Ar*, which promotes the reaction [19,49]. Meanwhile, we observed that the characteristic spectra of CH_2· and CH_3· were absent in the spectral images of this experiment. It is possibly due to these reactive particles being produced in very small quantities and with very short lifetimes under the experimental conditions, hence their absence in the characteristic spectral images. Additionally, during the discharge process, the characteristic spectra revealed that atomic carbon and ionic carbon underwent complex reactions to produce C II, C III, C IV, and C MIX.

2.5.2. Density functional theory analysis

To further elucidate the influence of microwaves on methane cracking processes, density functional theory (DFT) was employed to investigate the effect of microwave-induced electric fields on methane dissociation over a tungsten (001) surface. The methane decomposition process involves two key stages: methane adsorption and dehydrogenation. As shown in Fig. 7(a), these steps exhibit similarities to dissociation mechanisms observed on other catalysts [50,51]. As shown in Fig. 7(c), the optimal adsorption structure for methane dissociation aligns with those reported for Pd-based systems [52]. As illustrated in Fig. 7(a)-(c), the microwave-induced electric field significantly impacts the initial dissociation of methane. As a negative electric field perpendicular to the surface, the positive field direction is defined in Fig. 7(a), methane exhibits enhanced adsorption on the tungsten surface, thereby facilitating dissociation. Furthermore, as shown in Fig. 7(b), the electric field promotes the dissociation process by modulating bond lengths between adsorbates, the substrate, and within the adsorbate itself. When the electric field strength increased from −0.6–0 V/Å, the adsorption energy rose from −0.40 to −0.21 eV, accompanied by an expansion of the adsorption distance from 2.27 to 2.38 Å. Conversely, reversing the electric field polarity (0 → −0.6 V/Å) further weakened the adsorption energy to −0.15 eV while extending the adsorption distance to 2.66 Å.

To further investigate whether W needles can still catalyze methane decomposition after forming WC at elevated temperatures, Fig. 7(d) presents the energy variations associated with the dissociation of different chemical species on the tungsten carbide (WC) surface. In contrast to the W surface, methane undergoes initial cleavage on WC to form CH_3*, after which its subsequent dissociation becomes significantly more difficult. Nevertheless, compared with the direct cleavage of CH_4 the dissociation of CH_3* on WC should still be considerably easier (see the dissociation energy barrier diagram in Fig. S9 of the Supporting Information). On the W surface, by comparison, the dissociation barrier increases markedly only after CH* formation. Fig. 7(e) and (f) further illustrate the temperature–free energy (T–ΔG) profiles of methane decomposition on W and WC surfaces, respectively, corroborating the above conclusion: at around 1500 K (see the temperature distribution diagram in Fig. S10 of the Supporting Information), CH* on the W surface tends not to dissociate further, and the WC surface exhibits similar behavior. This observation suggests that CH* species may undergo polymerization to produce C2 products.

Based on our experimental results, we have observed a high selectivity for C2 products as well as a certain degree of carbon selectivity. These findings provide crucial clues about the surface state of the tungsten needle. Specifically, we need to combine experimental data to infer whether the surface of the tungsten needle remains pure tungsten (W) or partially transforms into tungsten carbide (WC).

Experimental data indicates that under various power settings, the selectivity for C2 products is high, suggesting that there are effective mechanisms for the generation and transformation of intermediates in the reaction pathway. Additionally, we have noted a certain level of carbon selectivity, indicating that some methane may not be converted into C2 products but instead is cracked to produce elemental carbon. If the surface of the tungsten needle remains pure tungsten (W), the primary intermediate generated would-be CH*. This singular intermediate generation pathway limits the formation of C2 products, leading to lower selectivity and yield for C2 products. In contrast, if the surface of the tungsten needle partially transforms into tungsten carbide (WC) during the reaction, a variety of intermediates, such as CH_3*, CH_2*, and CH*, may be generated. These intermediates are more likely to further react under high temperatures and plasma conditions to produce C2 products, thereby enhancing the selectivity and yield of C2 products. Furthermore, the WC surface has higher catalytic activity, which can promote the generation and transformation of various intermediates, favoring the production of C2 products over carbon.

Based on the above analysis, we can reasonably infer that under the current microwave conditions, the surface of the tungsten needle has partially transformed into tungsten carbide (WC). This conclusion is drawn from the following points: first, a C2 selectivity of around 50 % suggests that there are multiple effective mechanisms for the generation and transformation of intermediates, which is consistent with the reaction characteristics of the WC surface. Second, the observed carbon selectivity in the experiments indicates that some methane undergoes complete cracking to form solid carbon and hydrogen gas, without fully participating in the formation of C2 products, which is more common on a W surface. Lastly, under high-temperature conditions, the surface of the tungsten needle may undergo dynamic changes, with some tungsten reacting with carbon to form WC. This change in surface state can explain the high C2 selectivity and certain degree of carbon selectivity observed in the experiments.

2.5.3. Reaction mechanism

A rational reaction mechanism for the MDP to achieve conversion of CH_4 is proposed, as illustrated in Fig. 8. The CH_4 decomposition process is categorized into three sequential stages: (a) plasma discharge excitation, (b) intermediate medium reaction, and (c) product generation. In the microwave field, free electrons in the tungsten needles accumulate at the tip of the needles, and when a certain density is reached, a breakdown discharge occurs. The arc carries high-energy electrons to impact the reactants, causing the reactants to excite and ionize. At the same time, the high-energy electrons impact the C-H bond, causing the C-H bond to break and realizing the cracking of methane. When the free radicals collide, new products are produced.

Specifically, under the influence of the microwave field, high-energy electron aggregation occurs at the tip of the tungsten needle. When the electric field strength at the needle's tip surpasses the dielectric breakdown threshold of the working gas, it triggers the emission of electrons from the nucleus, thereby exciting the MDP. The excitation process primarily involves the excitation of Ar (See Table.S3(R2-R3)).

The intermediate reactions predominantly involve the activation of CH_4 to induce dissociation and the generation of free radicals. The initiation step of these intermediate reactions is the electron collision with CH_4(See Table.S3(R4-R9)). The activation of the C-H bond in CH_4 is primarily due to the energetic electrons produced by the MDP, as referenced in studies [19,53–55]. Additionally, the excited state of Ar, being a heavier species, also collides with methane, leading to the initial dissociation of CH_4 and the formation of CH_3 radicals. Concurrently, the heavy particles and electrons impact the resulting radicals, leading to the production of CH_2·, CH·, and free carbon (See Table.S3(R10-R22)). This is consistent with the results measured by the OES [54].The product generation stage is primarily the recombination of free radicals. The free radicals and particles generated during the intermediate reactions continue to collide, with CH_3 radicals playing a predominant role in these collision reactions (See Table.S3(R23-R46)). The interaction of different free radicals (CH_3·) and particles (Ar) results in the production of various products, culminating in the formation of new molecules [54,56].

Furthermore, we have observed the one-way reaction pathways of C2 hydrocarbons as reported in previous studies [54,56], which provides a compelling explanation for the dominant selectivity of C_2H_6 in this study. The shorter residence time is a determining factor for the high

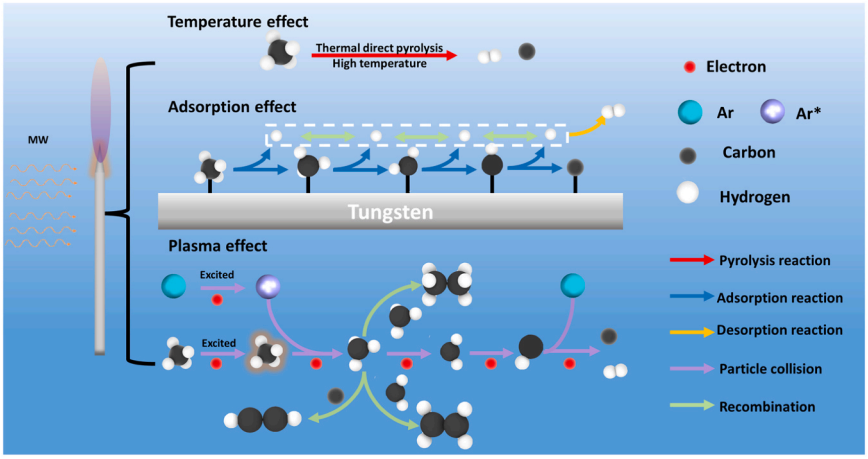

Fig. 8. Mechanism of CH_4 conversion by tungsten needle enhanced MDP.

selectivity of C_2H_2.

Fig. 9 and Table 2 show a comparison of various methane pyrolysis methods, namely the microwave plasma torch (MPT) [57], the dielectric barrier discharges (DBD) [53], the gliding arch plasma (GAP) [57] and the MDP (this work). Compared to MPT, DBD, and GAP, results of the MDP on the methane conversion, the hydrogen selectivity and SER are superior than other techniques. The MDP is an avenue for converting high concentrations of methane with low energy consumption. In those cases, a leading position is achieved in terms of the balance between methane conversion and energy consumption via the MDP strategy.

The comparison of methane cracking performance with different methods is shown in Table 2. The results indicate that this work also possesses good performance compared with other technologies.

Our research indicates that the microwave plasma-driven pyrolysis of methane holds significant potential for the production of high-purity hydrogen and solid carbon without CO_2 emissions. The rapid startup and shutdown capabilities, high conversion efficiency, and scalability of microwave technology offer substantial advantages for modular production, effectively reducing costs and enhancing resource efficiency. However, the tungsten needle electrodes may be affected by carbon deposition, which can impact the plasma generation efficiency and equipment stability over time. Future research should focus on developing technologies to prevent and remove carbon deposition. By continuously optimizing reaction parameters and improving operating conditions, the economic viability and practicality of this technology can be further enhanced to meet the demands of future energy markets. Thermal decomposition of methane achieves a conversion rate of 85 %, while catalytic decomposition of methane can reach a conversion rate of 92 %. However, compared to the 97 % conversion rate that we have already achieved in our research, there is still a gap. In contrast, the conversion rate of pyrolysis in a molten media is the lowest, at only 6 %.

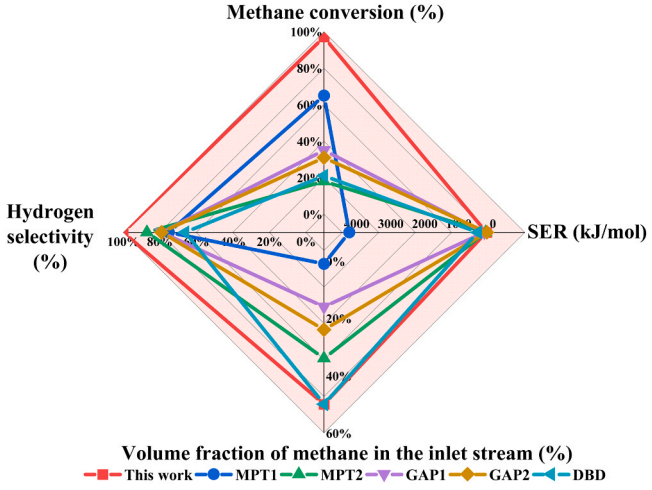

Fig. 9. Radar chart comparing results of different forms of plasma methane pyrolysis technologies.

Table 2
Comparison of different forms of methane pyrolysis technology.

Methodology	Methane Conversion (%)	Hydrogen Selectivity (%)	Volume fraction of methane in the inlet stream (%)	SER (kJ/mol)	Reference
MDP	97 %	100 %	50 %	180	This work
MPT1	65 %	75 %	1 %	4207	[57]
MPT2	18 %	87 %	34 %	198	
GAP1	35 %	79 %	16 %	239	
GAP2	31 %	79 %	24 %	164	
DBD	21 %	66 %	50 %	429	[53]
Thermal	85 %	/	/	/	[12]
Catalytic	92 %	/	/	/	[3]
Molten Media	6 %	/	/	/	[58]

3. Conclusions

In this study, a new MDP technique was proposed to pyrolyze methane into carbon-negative hydrogen and high-quality carbon material. The effects of key factors on CH_4 decomposition were comprehensively investigated, and its mechanisms under MDP atmosphere was illustrated. Under 300 W and 100 ml/min of 10 % CH4 and 90 % Ar, methane conversion and hydrogen production for SiC and CAC initially increased then decreased with bed height, reaching 4 % and 15 % respectively. Tungsten needles achieved 97 % conversion with continuous discharge in methane, up from intermittent in pure Ar. Key MDP parameters include power, flow rate, gas ratio, and diameter ratio. With tungsten needles, methane conversion ranged from 80 % to 99 %, and hydrogen selectivity from 35 % to 99 %. Power, though not significantly affecting conversion, influenced product distribution, yielding more hydrogen and solid carbon at higher levels. The best carbon product quality was observed at 400 W and 100 ml/min. Minimum specific energy requirements were 40 kJ/mol for methane conversion and 76 kJ/mol for hydrogen generation. HRTEM and Raman spectroscopy confirmed the production of few-layer graphene, demonstrating the effectiveness of methane pyrolysis for graphene production. OES and

DFT revealed that high-energy electrons and a strong electric field in the discharge region facilitate methane adsorption and C-H bond cleavage, enabling decomposition. Radical collisions in the reaction zone generate new products through recombination. Future research should conduct a more detailed composition analysis of multi-component natural gas and explore the application potential of solid carbon products in energy storage and environmental sustainability strategies. Despite the limitations, our study provides important insights for understanding and optimizing the process of producing hydrogen and solid carbon from natural gas, highlighting the key potential of microwave plasma technology in the energy sector.

CRediT authorship contribution statement

Wenshuo Wang: Writing – original draft, Formal analysis, Data curation. **Zhoulin Liu:** Software. **Baoxu Zhang:** Validation, Methodology. **Yuanyuan Lin:** Validation. **Xiaolong Wang:** Validation. **Liang Wang:** Writing – review & editing. **Jing Sun:** Methodology. **Tao Wang:** Methodology. **Xinyan Zhang:** Methodology. **Yingping Pang:** Conceptualization. **Xiqiang Zhao:** Conceptualization. **Yanpeng Mao:** Conceptualization. **Zhanlong Song:** Conceptualization. **Wenlong Wang:** Supervision. **Yinghe Zhang:** Supervision. **Ziliang Wang:** Writing – review & editing, Supervision, Methodology, Funding acquisition.

Declaration of Competing Interest

The authors declare that they have no known competing financial interests or personal relationships that could have appeared to influence the work reported in this paper.

Acknowledgments

This work was generously supported by Shandong Province Excellent Youth Science Fund Project (2023HWYQ-022), Jinan Science and Technology Project of Principal Investigator Workroom (202333057), National Natural Science Foundation of China (52476207, 52176203), Taishan Scholars Youth Expert Program of Shandong Province (tsqn202312002). The scientific calculations in this paper have been done on the HPC Cloud Platform of Shandong University. And we gratefully acknowledge the technical support from Dr. Shouyan Chen, Dr. Guifang Chen, and Ping Zhou of Shandong University for this work.

Appendix A. Supporting information

Supplementary data associated with this article can be found in the online version at doi:10.1016/j.jaap.2025.107473.

Data availability

Data will be made available on request.

References

[1] L. Duan, R. Petroski, L. Wood, K. Caldeira, Stylized least-cost analysis of flexible nuclear power in deeply decarbonized electricity systems considering wind and solar resources worldwide, Nat. Energy 7 (2022) 260–269.
[2] W. Wang, Green energy and resources: advancing green and low-carbon development, Green. Energy Resour. 1 (2023) 100009.
[3] S. Bazri, C. Mapelli, L.G. Mapelli, D. Mombelli, M.M.S. Tommasini, A. Lucotti, Thermo-catalytic methane pyrolysis for sustainable carbon production in steelmaking applications: stainless steel catalysis and CO_2-enhanced catalyst regeneration, J. Anal. Appl. Pyrolysis 192 (2025) 107334.
[4] C. Smith, L. Torrente-Murciano, Cost efficiency versus energy utilization in green ammonia production from intermittent renewable energy, Nat. Chem. Eng. 2 (2025) 261–272.
[5] J. Li, J. Lin, J. Wang, X. Lu, C.P. Nielsen, M.B. McElroy, et al., Redesigning electrification of China's ammonia and methanol industry to balance decarbonization with power system security, Nat. Energy 10 (2025) 762–773.
[6] O. Khalifeh, H. Taghvaei, A. Mosallanejad, M.R. Rahimpour, A. Shariati, Extra pure hydrogen production through methane decomposition using nanosecond pulsed plasma and Pt–Re catalyst, Chem. Eng. J. 294 (2016) 132–145.
[7] Y. Nishida, H.C. Chiang, T.C. Chen, C.Z. Cheng, Efficient production of hydrogen by DBD type plasma discharges, IEEE Trans. Plasma Sci. 42 (2014) 3765–3771.
[8] R. Kothari, D. Buddhi, R.L. Sawhney, Comparison of environmental and economic aspects of various hydrogen production methods, Renew. Sustain. Energy Rev. 12 (2008) 553–563.
[9] M. Plevan, T. Geißler, A. Abánades, K. Mehravaran, R.K. Rathnam, C. Rubbia, et al., Thermal cracking of methane in a liquid metal bubble column reactor: Experiments and kinetic analysis, Int. J. Hydrog. Energy 40 (2015) 8020–8033.
[10] J.D. Holladay, J. Hu, D.L. King, Y. Wang, An overview of hydrogen production technologies, Catal. Today 139 (2009) 244–260.
[11] J. Song, S. Park, Review of methane pyrolysis for clean turquoise hydrogen production, J. Anal. Appl. Pyrolysis 183 (2024) 106727.
[12] Z. Wang, W. Fan, G. Zhang, S. Dong, Exergy analysis of methane cracking thermally coupled with chemical looping combustion for hydrogen production, Appl. Energy 168 (2016) 1–12.
[13] D. Xue, P. Zhang, Y. Lin, W. Wang, J. Shi, Q. Hu, et al., Parametric study of the decomposition of methane for COx-free H2 and high valued carbon using Ni-based catalyst via machine-learning simulation, Green. Energy Resour. 3 (2025) 100114.
[14] A. Mašláni, M. Hlína, M. Hrabovský, P. Křenek, V.S. Sikarwar, J. Fathi, et al., Impact of natural gas composition on steam thermal plasma assisted pyrolysis for hydrogen and solid carbon production, Energy Convers. Manag. 297 (2023) 117748.
[15] A. Bogaerts, E.C. Neyts, Plasma technology: an emerging technology for energy storage, ACS Energy Lett. 3 (2018) 1013–1027.
[16] Y. Miao, A. Yokochi, G. Jovanovic, S. Zhang, A. von Jouanne, Application-oriented non-thermal plasma in chemical reaction engineering: a review, Green. Energy Resour. 1 (2023) 100004.
[17] Y. Guan, G. Song, C. Li, K.H. Lim, S. Das, P. Sarkar, et al., Recent progress in single-atom catalysts for thermal and plasma-assisted conversion of methane, Energy Convers. Manag. 325 (2025) 119390.
[18] M. Singh, A. Sengupta, K. Zeller, G. Skoptsov, R.L. Vander Wal, Effect of hydrogen concentration on graphene synthesis using microwave-driven plasma-mediated methane cracking, Carbon 143 (2019) 802–813.
[19] H. Zhang, C. Du, A. Wu, Z. Bo, J. Yan, X. Li, Rotating gliding arc assisted methane decomposition in nitrogen for hydrogen production, Int. J. Hydrog. Energy 39 (2014) 12620–12635.
[20] M. Wen, Y. Liu, J. Ren, J. Wang, J. Jiang, Optimizing microwave frequencies for hydrogen and electromagnetic shielding materials production through methane pyrolysis over biochar, Energy Convers. Manag. 309 (2024) 118430.
[21] H.M. Nguyen, F. Gorky, S. Guthrie, J.M. Crawford, M.A. Carreon, J.B. Jasinski, et al., Plasma catalytic non-oxidative methane conversion to hydrogen and value-added hydrocarbons on zeolite 13X, Energy Convers. Manag. 286 (2023) 117082.
[22] F. Zhang, X. Zhang, Z. Song, X. Li, X. Zhao, J. Sun, et al., Promotion of microwave discharge over carbon catalysts for CO_2 reforming of CH_4 to syngas, Fuel 331 (2023) 125914.
[23] Z. Xu, N. Gao, Y. Ma, W. Wang, C. Quan, X. Tu, et al., Biomass volatiles reforming by integrated pyrolysis and plasma-catalysis system for H_2 production: Understanding roles of temperature and catalyst, Energy Convers. Manag. 288 (2023) 117159.
[24] B. Zhang, Z. Song, Y. Pang, X. Zhang, J. Zhang, Y. Mao, et al., Tungsten-needle intensifies microwave-sustained plasma accelerating direct H_2S conversion to H_2, J. Hazard. Mater. 478 (2024) 135487.
[25] W. Fu, W. Zhang, Microwave-enhanced membrane filtration for water treatment, J. Membr. Sci. 568 (2018) 97–104.
[26] J. Fathi, M. Hlína, T. Mates, M. Buryi, V.S. Sikarwar, R. Mušálek, et al., Thermo-Chemical recycling of polypropylene via high-power microwave plasma gasification: syngas and metal carbide production, Chem. Eng. J. 511 (2025) 161910.
[27] S. Nomura, H. Toyota, S. Mukasa, H. Yamashita, T. Maehara, A. Kawashima, Production of hydrogen in a conventional microwave oven, J. Appl. Phys. 106 (2009) 073306.
[28] J. Sun, W. Wang, Q. Yue, C. Ma, J. Zhang, X. Zhao, et al., Review on microwave–metal discharges and their applications in energy and industrial processes, Appl. Energy 175 (2016) 141–157.
[29] B. Zhang, Z. Song, Y. Pang, J. Zhang, X. Zhao, Y. Mao, et al., High conversion of H_2S to H_2 and S via a robust microwave-induced discharge plasma, J. Clean. Prod. 435 (2024) 140588.
[30] S. Tian, W. Deng, Y. Su, Experimental study on single-mode microwave-induced tungsten wire discharge for NO conversion in NO/N_2 atmosphere, Environ. Sci. Pollut. Res 28 (2021) 19094–19106.
[31] J. Sun, Q. Wang, W. Wang, Z. Song, X. Zhao, Y. Mao, et al., Novel treatment of a biomass tar model compound via microwave-metal discharges, Fuel 207 (2017) 121–125.
[32] Z. Hussain, K.M. Khan, K. Hussain, Microwave–metal interaction pyrolysis of polystyrene, J. Anal. Appl. Pyrolysis 89 (2010) 39–43.
[33] G. Whittaker, D.M. Mingos, Arcing and other microwave characteristics of metal powders in liquid systems, J. CHEM. SOC. DALTON TRANS. J. CHEM SOC DALTON TRANS 2000 (2000) 1521–1526.
[34] W. Chen, B. Gutmann, C.O. Kappe, Characterization of microwave-induced electric discharge phenomena in metal–solvent mixtures, ChemistryOpen 1 (2012) 39–48.
[35] X. Li, C. Pang, H. Li, X. Gao, Microwave energy inductive fluidized metal particles discharge behavior and its potential utilization in reaction intensification, Chin. J. Chem. Eng. 33 (2021) 256–267.

[36] H. Zhu, Y. Huang, S. Yin, W. Zhang, Microwave plasma setups for CO_2 conversion: a mini-review, Green. Energy Resour. 2 (2024) 100061.
[37] R. Vander Wal, A. Sengupta, E. Musselman, G. Skoptsov, Microwave-driven plasmamediated methane cracking: product carbon characterization, C 4 (2018) 61.
[38] T. Minea, D.C.M. van den Bekerom, F.J.J. Peeters, E. Zoethout, M.F. Graswinckel, M.C.M. van de Sanden, et al., Non-oxidative methane coupling to C_2 hydrocarbons in a microwave plasma reactor, Plasma Process. Polym. 15 (2018) e1800087.
[39] S. Hamzehlouia, S.A. Jaffer, J. Chaouki, Microwave heating-assisted catalytic dry reforming of methane to syngas, Sci. Rep. 8 (2018) 8940.
[40] C. Bao, A. Serrano-Lotina, M. Niu, R. Portela, Y. Li, K.H. Lim, et al., Microwave-associated chemistry in environmental catalysis for air pollution remediation: a review, Chem. Eng. J. 466 (2023) 142902.
[41] L. Rachdi, V. Sushkov, M. Hofmann, Optical emission spectroscopy diagnostics for plasma parameters investigation in a Duo-Plasmaline surface-wave sustained discharge, Spectrochim. Acta Part B At. Spectrosc. 194 (2022) 106432.
[42] Kramida A., Yu Ralchenko, Reader J., and NASDT NIST Atomic Spectra Database (ver. 5.12), [Online]. Available: https:/ /physics.nist.gov/asd [2025, April 30]. National Institute of Standard s and Technology, Gaithersburg, MD.
[43] F. Tuitje, Martínez, P. Gil, T. Helk, J. Gautier, F. Tissandier, J.P. Goddet, et al., Nonlinear ionization dynamics of hot dense plasma observed in a laser-plasma amplifier, Light Science Applications 9 (2020) 187.
[44] O. Khalifeh, A. Mosallanejad, H. Taghvaei, M.R. Rahimpour, A. Shariati, Decomposition of methane to hydrogen using nanosecond pulsed plasma reactor with different active volumes, voltages and frequencies, Appl. Energy 169 (2016) 585–596.
[45] S. Zhang, Y. Gao, H. Sun, H. Bai, R. Wang, T. Shao, Time-resolved characteristics and chemical kinetics of non-oxidative methane conversion in repetitively pulsed dielectric barrier discharge plasmas, J. Phys. D Appl. Phys. 51 (2018) 274005.
[46] D. Graf, F. Molitor, K. Ensslin, C. Stampfer, A. Jungen, C. Hierold, et al., Spatially resolved raman spectroscopy of single- and few-layer graphene, Nano Lett. 7 (2007) 238–242.
[47] B. Pacakova, T. Verhagen, M. Bousa, U. Hübner, J. Vejpravova, M. Kalbac, et al., Mastering the wrinkling of self-supported graphene, Sci. Rep. 7 (2017) 10003.
[48] S.J. Chae, F. Güneş, K.K. Kim, E.S. Kim, G.H. Han, S.M. Kim, et al., Synthesis of large-area graphene layers on poly-Nickel substrate by chemical vapor deposition: wrinkle formation, Adv. Mater. 21 (2009) 2328–2333.
[49] B. Huang, C. Zhang, H. Bai, S. Zhang, K. Ostrikov, T. Shao, Energy pooling mechanism for catalyst-free methane activation in nanosecond pulsed non-thermal plasmas, Chem. Eng. J. 396 (2020) 125185.
[50] D. Tian, C. Zeng, H. Wang, X. Cheng, Y. Zheng, C. Xiang, et al., Effect of transition metal Fe adsorption on CeO_2 (110) surface in the methane activation and oxygen vacancy formation: a density functional theory study, Appl. Surf. Sci. 416 (2017) 547–564.
[51] C. Thierfelder, M. Witte, S. Blankenburg, E. Rauls, W.G. Schmidt, Methane adsorption on graphene from first principles including dispersion interaction, Surf. Sci. 605 (2011) 746–749.
[52] C.J. Zhang, P. Hu, Methane transformation to carbon and hydrogen on Pd(100): pathways and energetics from density functional theory calculations, J. Chem. Phys. 116 (2002) 322–327.
[53] R. Liu, Y. Hao, T. Wang, L. Wang, A. Bogaerts, H. Guo, et al., Hybrid plasma-thermal system for methane conversion to ethylene and hydrogen, Chem. Eng. J. 463 (2023) 142442.
[54] H. Zhang, W. Wang, X. Li, L. Han, M. Yan, Y. Zhong, et al., Plasma activation of methane for hydrogen production in a N_2 rotating gliding arc warm plasma: a chemical kinetics study, Chem. Eng. J. 345 (2018) 67–78.
[55] P. Chawdhury, S. Bhanudas Rawool, M. Umamaheswara Rao, C. Subrahmanyam, Methane decomposition by plasma-packed bed non-thermal plasma reactor, Chem. Eng. Sci. 258 (2022) 117779.
[56] A. Indarto, N. Coowanitwong, J.-W. Choi, H. Lee, H.K. Song, Kinetic modeling of plasma methane conversion in a dielectric barrier discharge, Fuel Process. Technol. 89 (2008) 214–219.
[57] S. Kreuznacht, M. Purcel, S. Böddeker, P. Awakowicz, W. Xia, M. Muhler, et al., Comparison of the performance of a microwave plasma torch and a gliding arc plasma for hydrogen production via methane pyrolysis, Plasma Process. Polym. 20 (2023) 2200132.
[58] B. Parkinson, C.F. Patzschke, D. Nikolis, S. Raman, D.C. Dankworth, K. Hellgardt, Methane pyrolysis in monovalent alkali halide salts: Kinetics and pyrolytic carbon properties, Int. J. Hydrog. Energy 46 (2021) 6225–6238.